We are IntechOpen,
the world's leading publisher of
Open Access books
Built by scientists, for scientists

4,800
Open access books available

122,000
International authors and editors

135M
Downloads

Our authors are among the

154
Countries delivered to

TOP 1%
most cited scientists

12.2%
Contributors from top 500 universities

CLARIVATE ANALYTICS
BOOK CITATION INDEX
INDEXED

WEB OF SCIENCE™

Selection of our books indexed in the Book Citation Index
in Web of Science™ Core Collection (BKCI)

Interested in publishing with us?
Contact book.department@intechopen.com

Numbers displayed above are based on latest data collected.
For more information visit www.intechopen.com

Nanostructured Indium Tin Oxides and Other Transparent Conducting Oxides: Characteristics and Applications in the THz Frequency Range

Ci-Ling Pan, Chan-Shan Yang, Ru-Pin Pan,
Peichen Yu and Gong-Ru Lin

Additional information is available at the end of the chapter

Abstract

Transparent conductors are essential for optoelectronic components operating in the far-infrared or terahertz (THz) frequency range. Indium tin oxide (ITO), extensively used in the visible, is semi-transparent in the far-infrared frequency range. Other types of bulk transparent conducting oxides (TCOs), such as aluminum-doped zinc oxide (AZO) and aluminum and ytterbium-doped zinc oxide (AYZO), have not yet been explored for THz applications. Recently, biomimic nanomaterials have been shown to exhibit exotic optical properties, e.g., broadband, omnidirectional antireflective properties. Indeed, nanostructured ITO was found to exhibit the above desirable characteristics. In this chapter, we describe the fabrication and characterization of several TCOs, including ITO nanomaterials and several types of bulk TCO thin films, e.g., AZO and AYZO. Performance of THz phase shifters with ITO nanomaterials as transparent electrodes and liquid crystals for functionalities is presented.

Keywords: terahertz, spectroscopy, transparent conducting oxides, indium tin oxide, nanostructures, nanorods, nanowhiskers, liquid crystals, far-infrared, millimeter wave, sub-millimeter wave, phase shifter, optoelectonics, ITO, AZO, AYZO

1. Introduction

Materials that exhibit good electrical conductivity and high optical transmittance are important in many applications. An interesting group of materials with these properties is known as transparent conducting oxides (TCOs) [1]. Among the TCOs, indium tin oxide (ITO) is one of the most frequently investigated. It is widely used as transparent electrodes in optoelectronic devices such as solar cells [2, 3]. Zinc oxide (ZnO), a well-known TCO, is a semiconductor with

wide band gap of about 3.3 eV at room temperature. Even after careful deposition procedure, the intrinsically doped ZnO films are still not well suited for applications because of their relatively high resistivity of about 10^{-2}–10^{-3} Ω cm and their instability at high temperature. Therefore, the extrinsic doping is necessary for lowering the resistivity. Zinc oxide films can be doped with metal ions such as aluminum (Al), chromium (Cr), gallium (Ga), and indium (In). Among these dopants, Al is relatively cheap, abundant and nontoxic. Thus, Al-doped ZnO (AZO) films are considered as low-cost substitutes for ITO films as transparent conducting films. AZO film has transparency higher than 80% and resistivity lower than 7×10^{-4} Ω cm and is comparable with the ITO film. Further, AZO films show high stability in hydrogen plasma during the fabrication process of amorphous silicon solar cells. In order to solve the degradation problem of AZO thin films, Al and ytterbium-doped ZnO (AYZO) is developed.

In view of emerging applications of terahertz (THz) technology, it is interesting to compare the THz performance of these TCO films and explore their potential use in THz optoelectronic devices. In the terahertz (THz) or far-infrared (FIR) frequency range, however, ITO exhibits high reflectance and strong absorption [2]. Recently, ITO nanocolumns have attracted a lot of attentions, because of its excellent optoelectronic and antireflection characteristics in the visible and near-infrared range [2, 3]. The successful development of ITO nanostructures as functional transparent electrodes relies on the clear understanding of their optical and electrical properties, which are linked to the structural properties. Unfortunately, previous studies mainly focused on preparation techniques and optical properties [4], except for our studies on mid- and far-infrared studies of the electrical characteristics of ITO thin films [5]. It was confirmed that this material is a good dichroic mirror for the FIR.

On the other hand, nanostructures of TCOs have attracted much attention. Recently, our group has confirmed that ITO nanomaterials, e.g., nanocolumn, nanorods, nanowires, and nanowhiskers (NWhs), exhibit superhydrophilicity as well as omnidirectional, broadband antireflective (AR) characteristics in the near-infrared and visible frequency range [6, 7]. These novel nanostructured TCOs have been employed successfully in devices such as light-emitting diodes (LEDs) and solar cells [8, 9]. Further, we showed that ITO NWhs are good conductors and highly transparent in the THz frequency range. The dielectric and conductive properties of these nanomaterials were investigated using THz time-domain spectroscopy (THz-TDS), which has been widely used to study the characteristics of novel materials, including metal thin films [10], nanostructure of ZnO [11] and CdSe quantum dots of various sizes [12].

In this chapter, we survey the frequency-dependent complex refractive indices and conductivities of several TCOs for their potential applications in the THz devices. TCOs studied include ITO nanomaterials, ITO sputtering films, AZO, and AYZO thin films. Besides, we will describe THz phase shifters employing ITO nanomaterials as transparent electrodes.

2. Preparation and characteristics of the transparent conducting oxides

2.1. ITO nanomaterials

Indium tin-oxide (ITO) nanorods and nanowhiskers were deposited on the high resistivity silicon substrate (499 μm) using glancing-angle electron-beam evaporation, and the nanostructures

were deposited on the microgrooved surface. The double-side-polished silicon substrate was attached to a holder, which was tilted at a deposition angle of 70° with respect to the incident vapor flux. There were seven holders which circle around the center of the chamber at a speed of 10 rpm during the deposition. The target source contained 5 wt % SnO_2 and 95 wt % In_2O_3. The chamber was first pumped down to a residue pressure of about 10^{-6} torr. Nitrogen gas is then injected at a flow rate at 1 sccm. This results in an oxygen-deficient atmosphere in the growth chamber. The working condition of the growth chamber was ~10^{-4} torr and 260°C. The tilted top view and cross-sectional scanning electron microscopy (SEM) images of the ITO nanorods are given in **Figure 1**) and those of nanowhiskers are given in **Figure 2**.

2.2. ITO sputtering thin films

Indium tin-oxide (ITO) thin films were grown on the high-resistivity silicon substrate at a temperature of 250°C using DC reactive magnetron sputtering. The target source composed of 5 wt.% SnO_2 and 95 wt.% In_2O_3. The magnetron operated at a power setting of about 300 W. While the film was being grown, argon and oxygen gas at flow rates of 20 and 0.4 sccm were injected such that the total pressure in the chamber was ~6 mtorr. All the
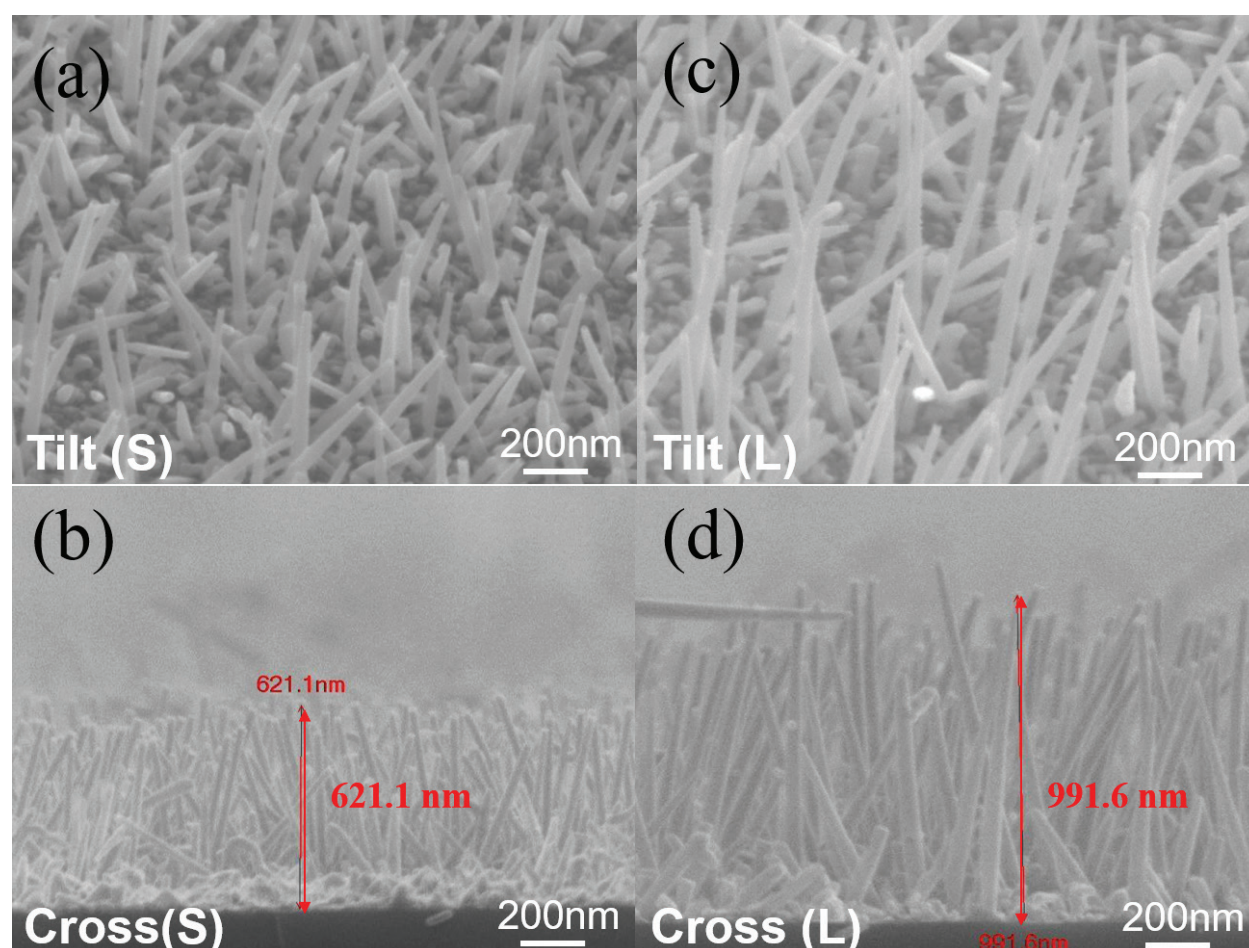
Figure 1. Tilted top view and cross-sectional scanning electron micrographs of ITO nanorods grown on silicon wafer with different lengths (a and b) 621.1 nm and (c and d) 991.6 nm. The scalar bars are 200 nm in length. Adapted from Ref. [13].
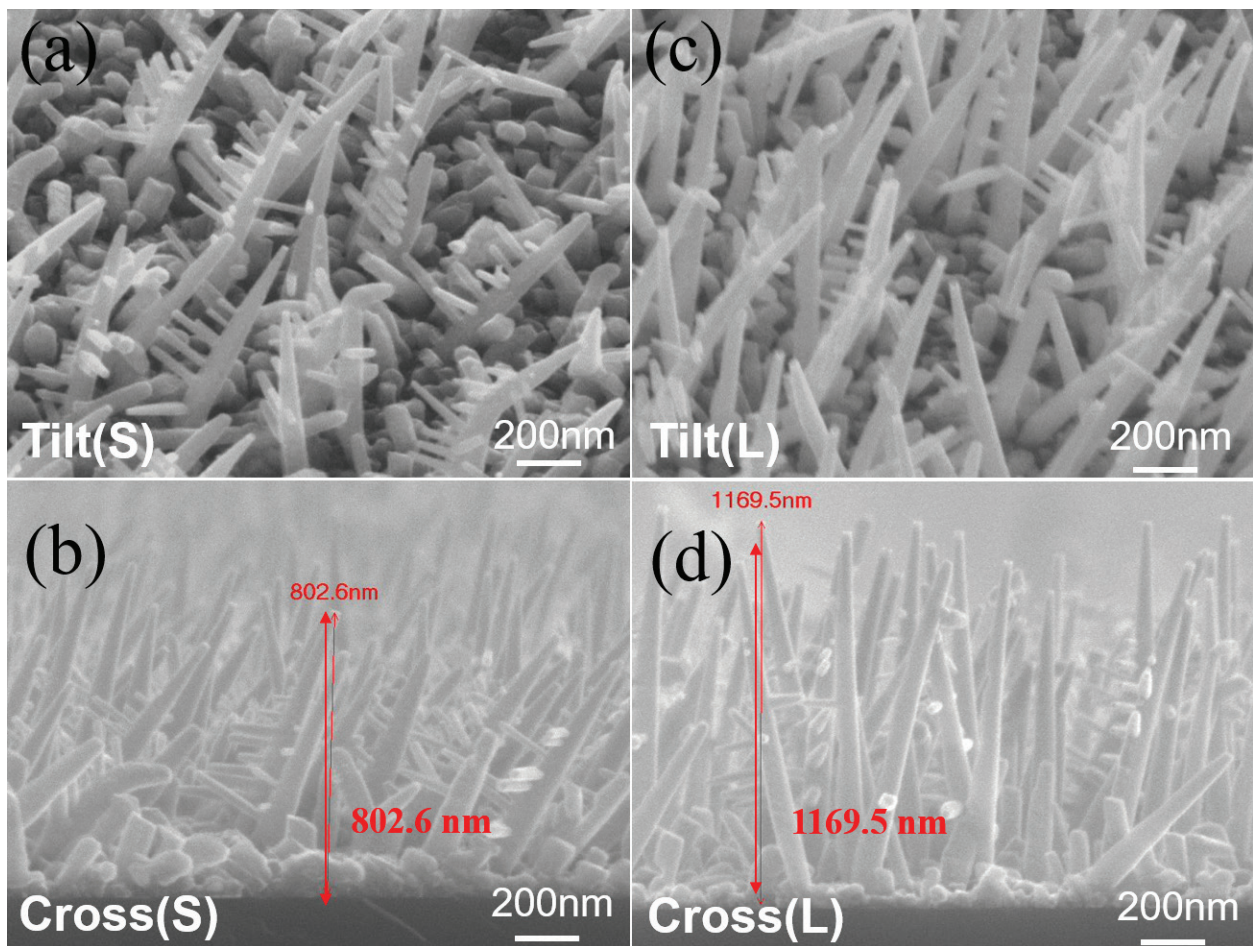
Figure 2. Tilted top view and cross-sectional scanning electron micrographs of ITO nanowhiskers grown on silicon wafer with different lengths (a and b) 802.6 nm and (c and d) 1169.5 nm. The scalar bars are 200 nm in length. Adapted from Ref. [13].

ITO thin films we studied were as-grown, not subject to further annealing. The thin films we studied were 333, 345, 615, and 1062 nm in thickness, as measured by an n&k Analyzer, model 1280.

2.3. AZO and AYZO thin films

All the AZO and AYZO films were deposited on undoped Si substrates by using the RF sputtering system. During the AZO process, the AZO target was composed of 98 wt.% ZnO and 2 wt.% Al. The chamber pressure and RF plasma power were controlled at 3 mtorr and 0.8 W/cm², respectively. The argon (Ar) fluence was fixed at 30 sccm during deposition. The AYZO target, on the other hand, was composed of 98 wt.% ZnO, 1 wt.% Al, and 1 wt.% Yb. The chamber pressure and magnetron plasma power were controlled at 3 mtorr and 0.896 W/cm², respectively. The chamber pressure and magnetron plasma power were set at 3 mtorr and 0.231 W/cm², respectively. The Ar and oxygen fluences were fixed at 12 and 1 sccm, respectively, during deposition process.

3. Experimental and analytical methods

3.1. Broadband THz time-domain spectroscopy (THz-TDS)

We employed several THz-TDS systems, including transmission and reflection types, among which the broadband system is shown in **Figure 3** as an example. In this system, we employed a commercial femtosecond Ti: sapphire laser system (Spectra Physics, Spitfire) as the light source, which provides 50 fs pulse duration at 815 nm central wavelength and 1.6 mJ pulse energy at 1 kHz. In the experimental setup, the incident beam is divided into the pump beam and probe beam by the beam splitter. Then, the collimated fundamental wave of the pump beam is focused on the focal point by the convex lens (with a focal length of f = 15 cm), and the intensity must be high enough to produce the plasma in the air. On the other hand, we use the 100-μm-thick β-barium-borate (BBO) crystal, which is cut so as to achieve type-I phase-matching for second-harmonic generation (SHG) of the 815 nm fundamental light, and the fundamental and second harmonic wave will form the asymmetric laser field. In other words, it means that electron is ionized by the fundamental and second-harmonic wave in the focal point. The ionized electrons in the plasma region are accelerated by the asymmetric laser field, which induces the electron oscillation. Subsequently, the THz wave is generated by the oscillation electron. The emitted THz radiation is collimated by an off-axis parabolic mirror with an effective focal length of f = 50.8 mm and then focused with a second one (also with f = 100.16 mm) onto the sample.The pump laser beam transmitted through the plasma region is blocked by the silicon wafer which has high transmissivity in the THz frequency region, while strongly absorbing the pump laser photons. Another pair of off-axis parabolic mirrors with the same focal length as that of the previous pair focus the THz signal into the detector. The resulting THz field was measured using an electro-optic sampling technique employing a 0.3-mm-thick GaP<110> crystal. The pellicle beam splitter which is transparent in THz frequency and the reflection is 40% in the 800 nm. In order to increase the signal-to-noise ratio (SNR), the chopper and lock-in amplifier are used. The frequency of chopper is about 500 Hz which is the most stable condition in our system. The translation stage scans the THz wave with 5 μm and total of 1024 steps. An antenna-based THz-TDS, as described in our previous works [2, 14, 15], was also employed. The spectroscopic characteristics of both systems are illustrated in Figure 2. Clearly, the two systems would allow us to study material properties in the band of 0.15–9.00 THz.

3.2. Extraction of optical parameters by THz-TDS

We extract the optical parameters of different kinds of materials by analyzing the THz waveform obtained from the THz-TDS. In this section, the method of extracting the frequency-dependent complex refractive index will be introduced. The process is achieved through the Fresnel equations and the multireflection approximation while numerical calculation is also applied.

The thin sample is grown on its substrate and its thickness is usually several micrometers or even several hundred nanometers. The time delays for thin samples whose thicknesses are of
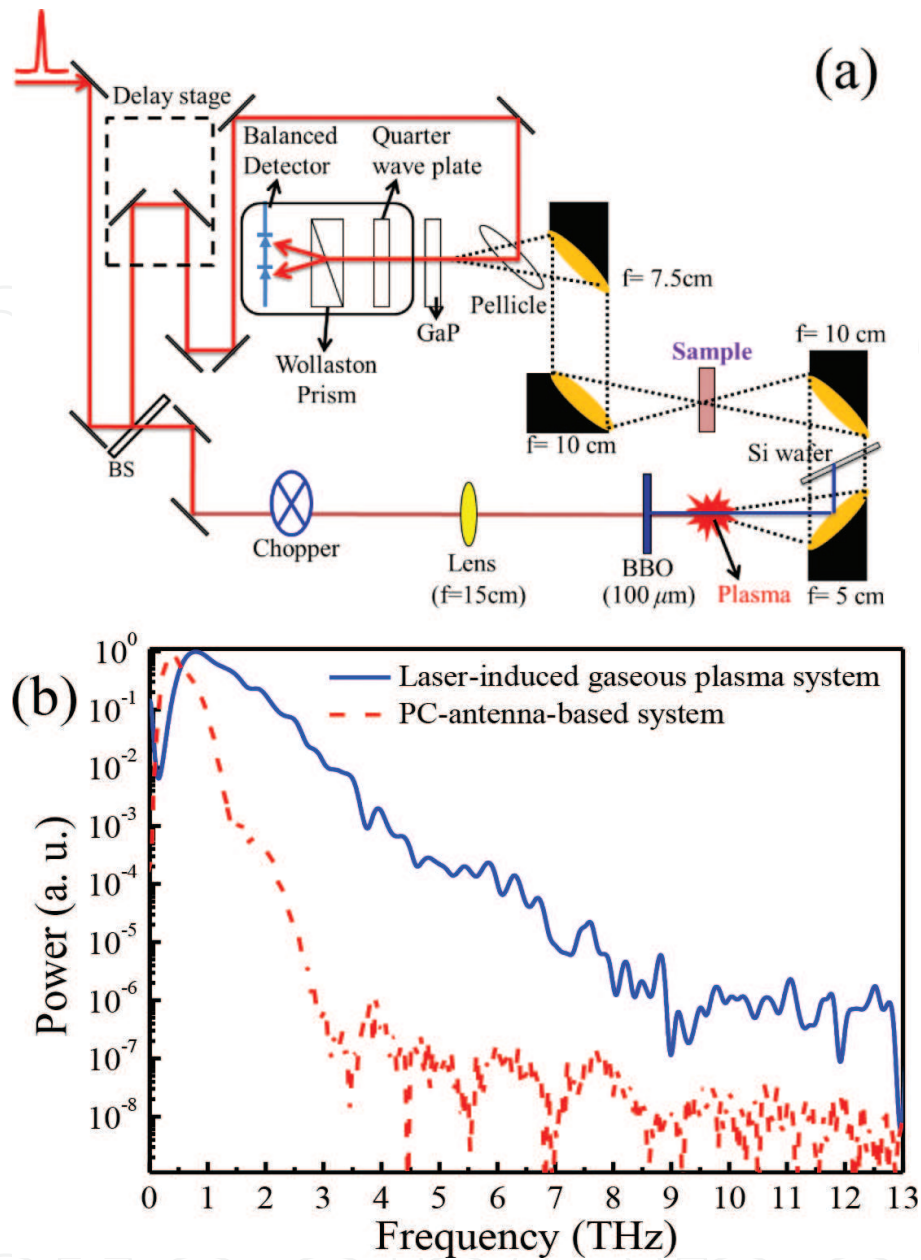
Figure 3. (a) Experimental setup of THz-TDS based on laser-induced gas plasma. (b) Typical performance of the THz-TDS systems based on laser-induced gaseous plasma (blue solid line) and PC antenna (red dash line) is shown. Adapted from Ref. [13].

the order of nanometers are smaller than 1 ps. Therefore, we are not able to distinguish the multireflected signal from the main signal. **Figure 4** shows that the main peak includes all multireflected signals which come from the thin sample layer and the second signal is caused by the reflection of the relatively thick substrate. In cases like this, we have to take multiple reflections into account in our analysis [5].

Schematic diagrams of electromagnetic model are shown in **Figure 5**. $E_0^*(\omega)$ is the incident THz field, and $E_{ref}^*(\omega)$ is the field which has passed through the substrate only. $E_{film}^*(\omega)$ is the field which has transmitted through the thin film sample including thin film layer and substrate
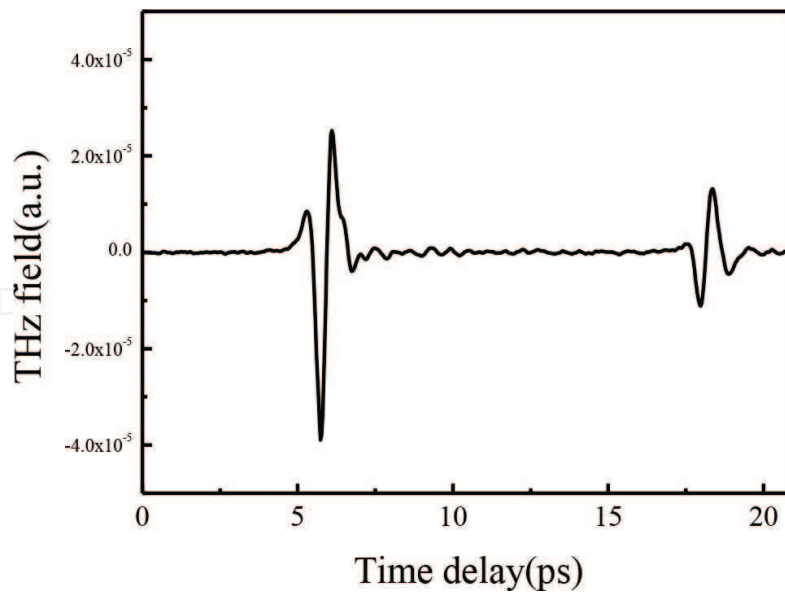
Figure 4. Transmitted THz waveform of 273 nm ITO thin film which is grown on fused silica substrate. The reflection signal appears behind the main signal for about 12 ps. The thickness of the substrate is 941 μm.
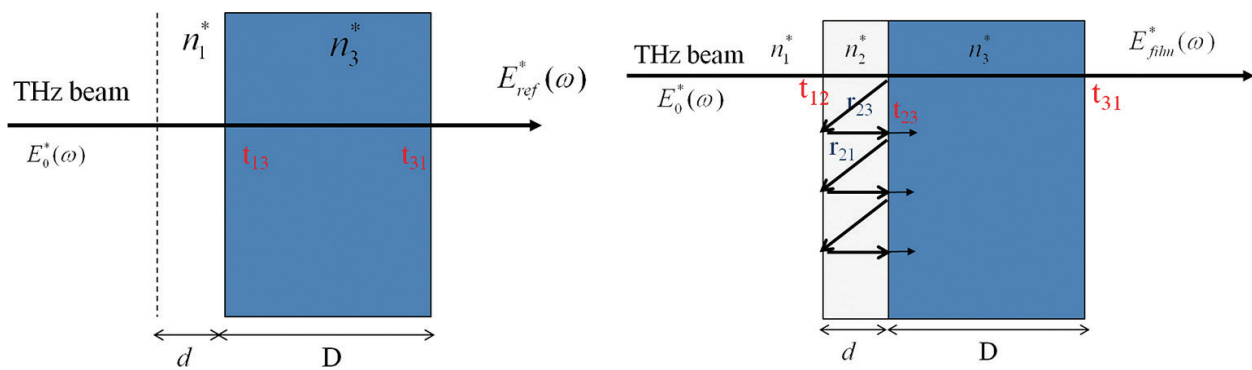
Figure 5. Schematic diagrams of electromagnetic model for reference and thin sample, respectively.

while the effect of multireflection is not considered here. $n_1^* = 1$, $n_2^* = n_2 + i \kappa_2$, and n_3^* are the refractive indices of air, thin film, and substrate, respectively. D is the thickness of the substrate and d is the sample layer. c_0 is the speed of light.

In our experimental setup, the THz pulse normally incidents the sample. Therefore, the well-known Fresnel equations of reflectance coefficient and transmittance coefficient can be expressed as the following equations:

$$t_{ij} = \frac{2\,n_i^*}{n_i^* + n_j^*} \tag{1}$$

$$r_{ij} = \frac{n_i^* - n_j^*}{n_i^* + n_j^*} \tag{2}$$

From Eq. (1) and (2), $E_{ref}^*(\omega)$ can be determined as the following equation.

$$E_{ref}^*(\omega) = E_0(\omega) \, t_{13} \, t_{31} \, e^{i\frac{n_1^*\omega d + n_3^*\omega D}{c}} \tag{3}$$

With the thin film layer, multireflection effect must be considered. The field which has passed through the thin film layer and is going to pass substrate layer can be noted as $E_{sample}^*(\omega)$. The field $E_{sample}^*(\omega)$ therefore has the relationship with $E_{film}^*(\omega)$ expressed as

$$E_{film}^*(\omega) = E_{sample}^*(\omega) \, t_{31} \, e^{i\frac{n_3^*\omega D}{c}} \tag{4}$$

$$E_{sample}^*(\omega) = E_0^*(\omega) \, t_{12} \, t_{23} \, e^{i\frac{n_2^*\omega d}{c}} + E_0^*(\omega) \, t_{12} \, r_{23} \, r_{21} \, t_{23} \, e^{i\frac{3n_2^*\omega d}{c}} + E_0^*(\omega) \, t_{12} \, r_{23}^2 \, r_{21}^2 \, t_{23} \, e^{i\frac{5n_2^*\omega d}{c}}$$
$$+ \cdots + E_0^*(\omega) \, t_{12} \, r_{23}^q \, r_{21}^q \, t_{23} \, e^{i\frac{(2q+1)n_2^*\omega d}{c}} \tag{5}$$

Here q is the number of multiple reflections. Assuming the number of multiple reflections is infinite ($q \to \infty$), the field $E_{sample}^*(\omega)$ can be simplified as

$$E_{sample}^*(\omega) = E_0^*(\omega) \, \frac{t_{12} \, t_{23} \, e^{i\frac{n_2^*\omega d}{c}}}{1 - r_{21} \, r_{23} \, e^{i\frac{2n_2^*\omega d}{c}}} \tag{6}$$

From Eqs. (3), (4), and (6), the theoretical complex transmittance can be determined.

$$T_{theo}^*(\omega) = \frac{E_{film}^*(\omega)}{E_{ref}^*(\omega)} = \frac{t_{12} \, t_{23} \, e^{i\frac{(n_2^*-1)\omega d}{c}}}{t_{13}\left(1 - r_{21} \, r_{23} \, e^{i\frac{2n_2^*\omega d}{c}}\right)} \tag{7}$$

Here t_{12}, t_{13}, t_{31}, t_{23}, r_{21}, and r_{23} are the Fresnel transmission and reflection coefficients which come from the Fresnel equations and are shown below.

$$t_{12} = \frac{2n_1^*}{n_1^* + n_2^*}, \; t_{23} = \frac{2n_2^*}{n_2^* + n_3^*}, \; t_{13} = \frac{2n_1^*}{n_1^* + n_3^*}, \; r_{23} = \frac{n_2^* - n_3^*}{n_2^* + n_3^*}, \text{ and } r_{21} = \frac{n_2^* - n_1^*}{n_2^* + n_1^*} \tag{8}$$

From the above-mentioned formulas, the theoretical complex transmittance can be determined. This model is utilized for extractions of complex refractive index for thin film grown on thick substrate.

In order to avoid the effect of difference of substrate thickness D between reference and sample, we have to modify the equations we use in the theoretical model. The concept of thickness correction is described in **Figure 6**. By modifying Eqs. (4) and (6), the transmitted field of the sample $E_{film}^*(\omega)$ (Eq. 9) can be derived when thickness correction is taken into account. While the transmitted field of reference $E_{ref}^*(\omega)$ is the same, we can conclude the theoretical complex transmittance $T_{theo}^*(\omega)$ (Eq. (10) by combining Eq. (3) and Eq. (9).

$$E_{film}^*(\omega) = E_0^*(\omega) \, \frac{t_{12} \, t_{23} \, t_{31} \, e^{i\frac{n_2^*\omega d}{c}}}{1 - r_{21} \, r_{23} \, e^{i\frac{2n_2^*\omega d}{c}}} \, e^{i\frac{n_1^*\omega\Delta d + n_3^*\omega(D-\Delta d)}{c}} \tag{9}$$

$$T_{theo}^*(\omega) = \frac{E_{film}^*(\omega)}{E_{ref}^*(\omega)} = \frac{t_{12} \, t_{23} \, e^{i\frac{(n_2^*-1)\omega d}{c}}}{t_{13}\left(1 - r_{21} \, r_{23} \, e^{i\frac{2n_2^*\omega d}{c}}\right) e^{i\frac{(n_3^*-1)\omega\Delta d}{c}}} \tag{10}$$
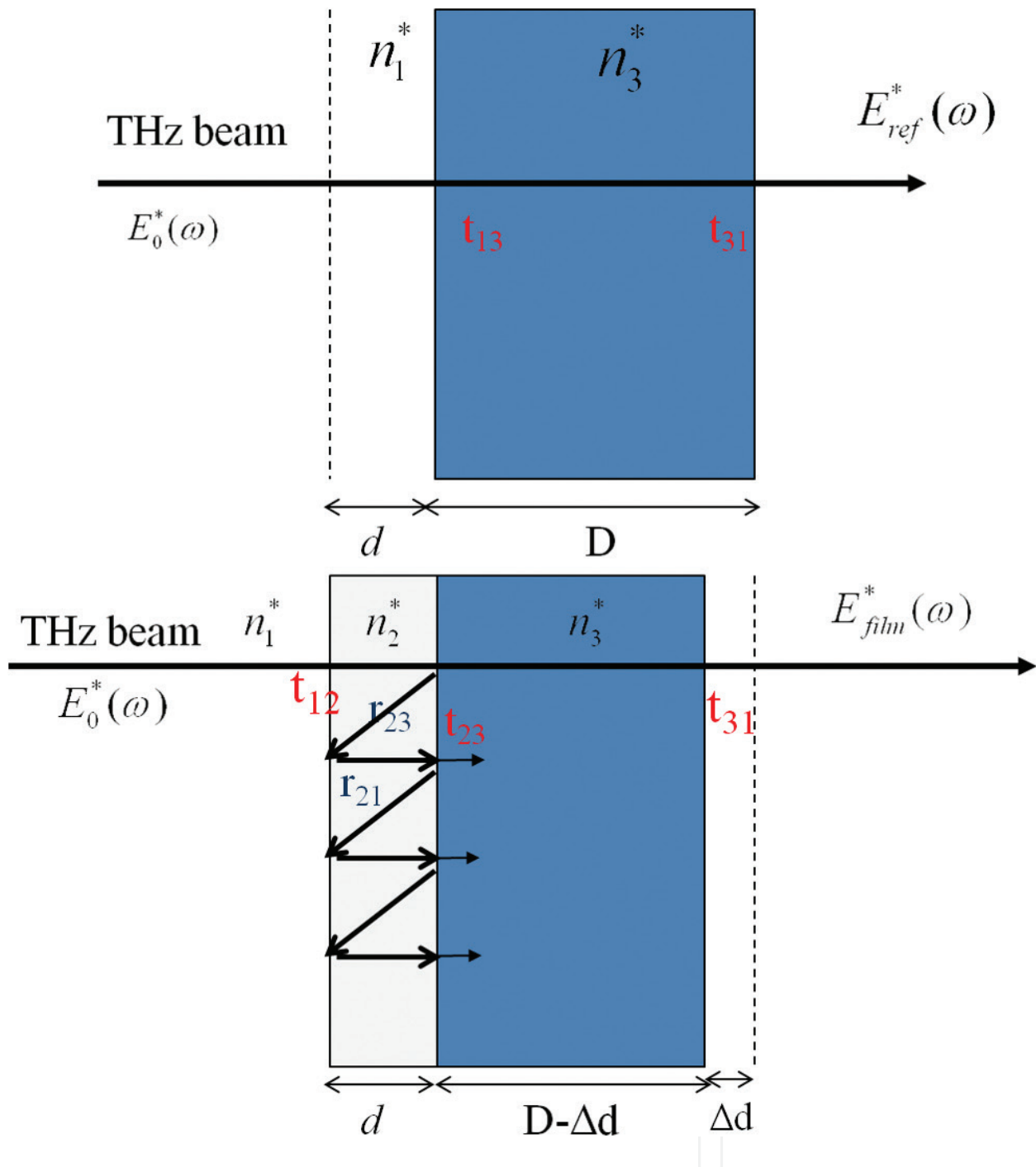
Figure 6. Schematic diagram of thickness correction.

We obtain the experimental data from THz time-domain spectroscopy. The experimental complex transmittance $T_{exp}^*(\omega)$ can be therefore derived.

$$T_{exp}^*(\omega) = \frac{E_{film}^*(\omega)}{E_{ref}^*(\omega)} \tag{11}$$

Here the complex fields $E_{film}^*(\omega)$ and $E_{ref}^*(\omega)$ are obtained from experimental data which are the results of transmitted THz pulse for sample and reference respectively. By comparing

the complex transmittance of theoretical and experimental results, the unknown frequency-dependent complex refractive index n_2^* of the thin film can be extracted. First of all, the error function between the theoretical and experimental complex transmittance is defined as Eq. (12). Because of the unknown refractive index n_2^*, the transmittance is dependent both on frequency and n_2^*.

$$\text{Error}(\omega, n_2^*) = \left| T_{\text{exp}}^*(\omega, n_2^*) - T_{\text{theo}}^*(\omega, n_2^*) \right| \tag{12}$$

$$\text{Find Minimum} = \left[\text{Error}(\omega, n_2^*) \right] \tag{13}$$

With the help of mathematical program, we may make the theoretical transmittance match the experimental transmittance to a minimum difference value by finding a suitable complex refractive index n_2^*. The index $n_2^* = n_2 + i\,\kappa_2$ therefore can be extracted.

3.3. Terahertz conductivity

For a nonmagnetic medium, the frequency-dependent dielectric constant is the square of the complex refractive index. In the following equations, ε^* is the complex dielectric constant with real and imaginary parts, i.e., ε_r, n and ε_i, κ are the real and imaginary parts of the refractive index, respectively, all functions of frequency.

$$\varepsilon^* = \varepsilon_r + i\,\varepsilon_i = (n + i\kappa)^2 \tag{14}$$

$$\varepsilon_r = n^2 - \kappa^2,\ \varepsilon_i = 2n\kappa \tag{15}$$

From the relationship mentioned above, the real and imaginary parts of dielectric constant are derived. Furthermore, the dielectric constant is related to the optical conductivity which will be fully described by the following paragraph.

Secondly, with several approximations, the Maxwell's equation can be modified into the form related to conductivity. We assume that the flowing current density has the form of $\vec{J} = \sigma^* \vec{E}$ (Ohm's law) where σ^* is complex conductivity. Also, the harmonic assumption for electric field $\vec{E}(\omega, t) = \vec{E_0} e^{-i\omega t}$, where $\vec{E_0}$ is the amplitude and ω and t represent frequency and time is applied. And the relation between displacement field and electric field $\vec{D} = \varepsilon_0\,\varepsilon_\infty \vec{E}$ is also used.

$$
\begin{aligned}
\nabla \times \vec{H} &= \vec{J} + \frac{\partial \vec{D}}{\partial t} = \vec{J} - i\omega\,\varepsilon_0\,\varepsilon_\infty \vec{E} \\
&= -i\omega\,\varepsilon_0\left[\varepsilon_\infty - \frac{\sigma^*}{i\omega\,\varepsilon_0}\right]\vec{E} \\
&= -i\omega\,\varepsilon_0\,\varepsilon^* \vec{E}
\end{aligned}
\tag{16}
$$

$$\varepsilon^* = \varepsilon_\infty + i\frac{\sigma^*}{\omega\,\varepsilon_0} \tag{17}$$

Here $\varepsilon_0 = 8.854 \times 10^{-12}$ (F/m) is the free-space permittivity. σ^* is complex conductivity, and ε^* and ε_∞ are the complex dielectric function and the dielectric constant, respectively. From Eq. (17), the complex conductivity can be derived:

$$\sigma^*(\omega) = \left(\sigma_r + i\,\sigma_i\right) = i\omega\,\varepsilon_0(\varepsilon_\infty - \varepsilon^*) \tag{18}$$

By substituting Eqs. (14) and (15) into Eq. (18), the complex conductivity's real and imaginary parts can be determined:

$$\sigma_r = \omega\,\varepsilon_0\,\varepsilon_i = 2n\kappa\omega\,\varepsilon_0 \tag{19}$$

$$\sigma_i = \omega\,\varepsilon_0(\varepsilon_\infty - \varepsilon_r) = \omega\,\varepsilon_0(\varepsilon_\infty - n^2 + \kappa^2) \tag{20}$$

The nanostructured ITO was considered as a composite material of ITO and air. The effective medium approximation (EMA) [16, 17] was assumed to be valid. We write the equivalent dielectric function of the nanostructured material of interest as

$$\varepsilon^*_{\text{Equivalent}} = f \times \varepsilon^*_m + \left(1 - f\right) \times \varepsilon^*_h \tag{21}$$

In Eq. (21), ε^*_m and ε^*_h are the dielectric constants of materials such as ITO and air, respectively, whereas f is the filling factor, i.e., the volume fraction of the nanomaterial in the composite. Similarly, the real (ε_{Re}) and imaginary (ε_{Im}) parts of the dielectric constants of pure nanostructured material can be written as

$$\varepsilon_{\text{Re}} = \left[n^2 - \kappa^2 - (1 - f)\right]/f \tag{22}$$

$$\varepsilon_{\text{Im}} = [2 \cdot n \cdot \kappa]/f \tag{23}$$

Finally, the real (σ_r) and imaginary (σ_i) parts of the complex conductivities of pure ITO nanostructures can be expressed in terms of the filling factors as

$$\sigma_r = \omega\,\varepsilon_0 \cdot (2n\kappa)/f \tag{24}$$

$$\sigma_i = \omega\,\varepsilon_0\left[\varepsilon_\infty - \left[n^2 - \kappa^2 - (1 - f)\right]/f\right] \tag{25}$$

Consequently, the complex conductivity can be acquired by THz-TDS and the analysis is just based on the most fundamental Fresnel equations and Maxwell's equation without any other complicated model.

### 3.4. Non-Drude behavior in terahertz conductivity

The Drude model was often used to analyze conductive properties of metals and bulk semi-conductors. In the model, the conductivity is given by $\sigma^*(\omega) = \varepsilon_0 \omega_p^2 \tau / (1 - i\omega\tau)$ [18]. In this expression, τ and ω_p are scattering times of carriers in the material and plasma frequency, respectively. According to the model, the real part of conductivity, Re{σ}, reaches its highest value when $\tau = 0$. This is the so-called DC conductivity. At higher frequencies, Re{σ} decreases because of the $1/\tau$ dependence. On the other hand, the value of Im{σ} is always positive. Its maximum occurs when the frequency is in the vicinity of the inverse of the scattering rate [18]. The THz conductivities of ITO nanostructures, however, exhibit non-Drude-like behavior, e.g., depressed values of DC conductivity and negative values for Im{σ}.

Therefore, the Drude-Smith model, which takes into account the carrier localization effect, is applied to fit the experimentally deduced conductivity of the ITO material [19, 20]. In this model, we write

$$\sigma^*(\omega) = \varepsilon_0 \omega_p^2 \tau \cdot \left[1 + \gamma / (1 - i\omega\tau)\right] / (1 - i\omega\tau) \tag{26}$$

where ω_p and τ are defined as plasma frequency and scattering time, respectively. Also in Eq. (26), the parameter γ is equal to the expectation value of cosine of carrier scattering angle. It gauges the persistence of velocity of carriers. The values of γ vary from 0 to 1. If $\gamma \approx 0$, the material shows Drude-like behavior. That is, the scattering of carriers is isotropic. In the limit of $\gamma = -1$, on the other hand, the carriers fully backscattered. The carrier localization effect is strong. We have conducted a simulation study of the complex conductivity of ITO nano-structures based on Drude-Smith model. The plasma frequency (ω_p) and scattering time (τ) are fitting parameters. The best fitted values for these two are found to be equal to 363 rad THz and 49 fs, respectively. The cases of $\gamma = 0$, $\gamma = -0.25$, $\gamma = -0.75$, and $\gamma = -1$ are shown in **Figure 7(a–d)**, respectively. If $\gamma = 0$, see **Figure 7(a)**, the Drude-Smith model reduces to the Drude-like model, which has been described previously. In short, the curves for Re{σ} and Im{σ} versus frequency exhibit maxima. Further, the value of Re{σ} decreases with increasing frequency. For the case of $\gamma = -0.25$ (see **Figure 7(b)**), both maximum values will show a little shift toward higher frequency. For the cases of $\gamma = -0.75$ and -1 (see **Figure 7(c and d)**), the complex conductivities of the nanometer exhibit other features, e.g., a minimum for Im{σ}. Further, there is an angular frequency at which Im{σ} crosses zero. As a result, the Im{σ} is negative from DC to the zero-crossing frequency. The maxima of Re{σ} now occurs at a nonzero frequency. There are some studies that attribute the non-Drude-like behavior to backscattering of carriers by grain boundaries [21–25]. In addition, after releasing free electrons, the dopants in n-type TCOs will become positive ions. Due to the Coulomb inter-action between free electrons and dopant ions, the latter will also act as scattering centers. Consequently, movement of the electrons will be further impeded [26, 27].

Armed with knowledge of ω_p and τ, the mobility (μ), carrier concentration (N_e), and DC con-ductivity (σ_0) of the material can then be calculated using the relations, $\mu = (1+\gamma)e\tau/m^*$, $N_e = \varepsilon_0 \omega_p^2 m^*/e^2$, and $\sigma_0 = \varepsilon_0 \omega_p^2 \tau (1+\gamma)$, respectively. In these expressions, $e = 1.602 \times 10^{-19}$ C, is the electronic charge; the electron effective mass is given by $m^* = 0.3 m_0$ [28], where $m_0 = 9.1094 \times 10^{-31}$ kg, is the electron's mass.
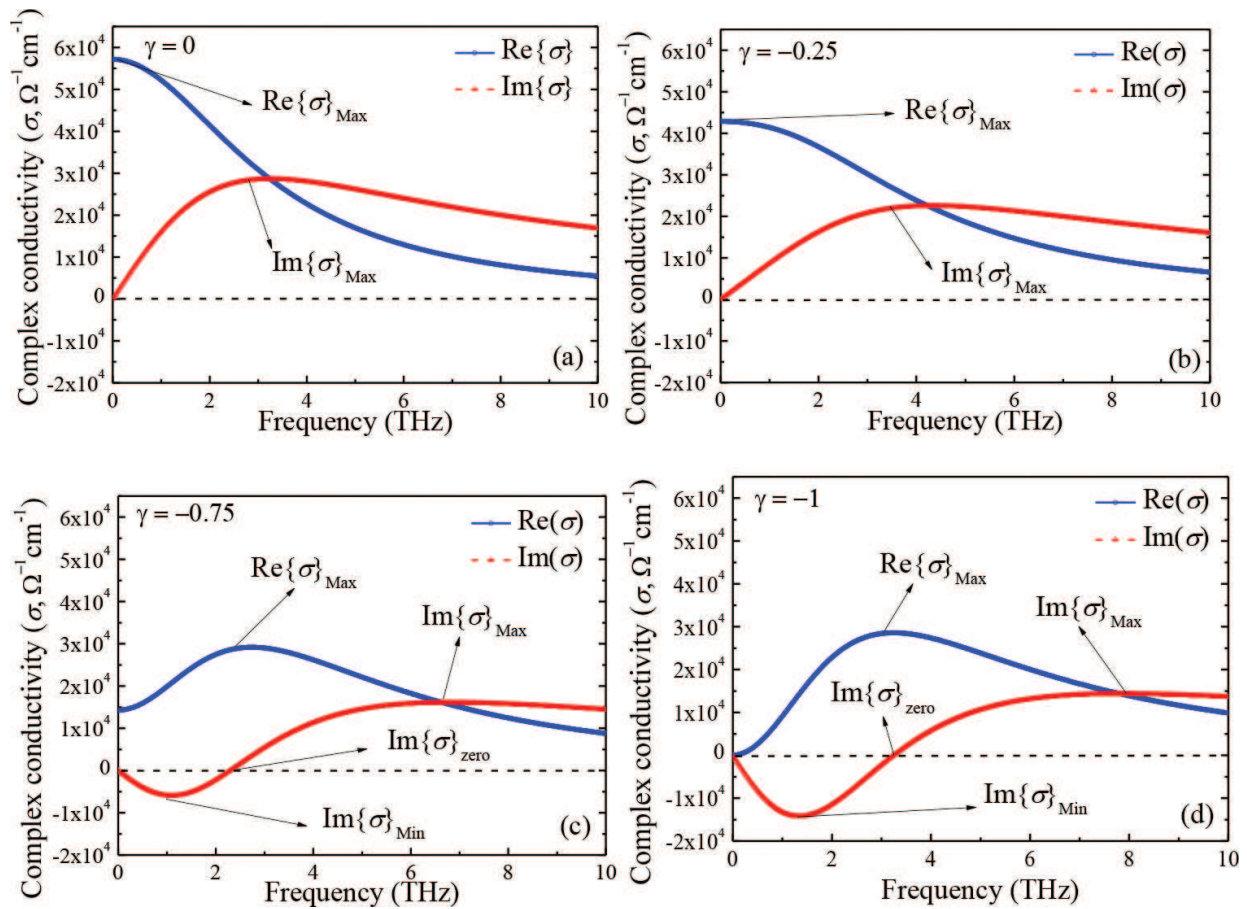
Figure 7. Simulation of the complex conductivities of ITO nanostructures using the Drude-Smith model for the cases of (a) $\gamma = 0$, (b) $\gamma = -0.25$, (c) $\gamma = -0.75$, and (d) $\gamma = -1$. From the fitting, the plasma frequency (ω_p) and scattering time (τ) are determined to be 363 rad THz and 49 fs, respectively.

4. THz optical constants and conductivities of selected TCOs

We have studied several TCOs using Fourier transform infrared spectroscopic (FTIR) and THz-TDS. First of all, the average transmittance of 100 nm thick ITO, AZO, and AYZO in the millimeter wave to submillimeter wave range was determined to be ~21%, ~48%, and ~28%, respectively. In **Figure 8(c)**, following the procedure detailed in Section 3 of the chapter, we found that the DC conductivity (σ_{DC}) and DC mobility (μ) for ITO thin films are 1.18–1.65 × 10^3 Ω^{-1} cm^{-1} and 96–120 cm^2 V^{-1} s^{-1}, respectively. In **Figure 8(a)** and **8(b)**, similarly, for AZO and AYZO thin films, σ_{DC} and μ are 0.41–1.06 × 10^3 Ω^{-1} cm^{-1} and 7–84 cm^2 V^{-1} s^{-1} versus 0.91–1.12 × 10^3 Ω^{-1} cm^{-1} and 26–85 cm^2 V^{-1} s^{-1}, respectively. Examining X-ray diffraction (XRD) data of these samples, we can immediately conclude that mobility of a particular sample is higher if the film exhibits larger grain size. On the other hand, if the carrier concentration (N_e) in the sample is high, the mobility of the sample would be lower as a result of the smaller distance between impurity ions. Our studies of these bulk TCO films to date thus indicate that AYZO has reasonable THz transmittance and electrical properties. Within this class, it may be the material of choice than ITO (lower THz transmittance) and AZO (lower mobilities) thin films for optoelectronic applications in the THz frequency range.
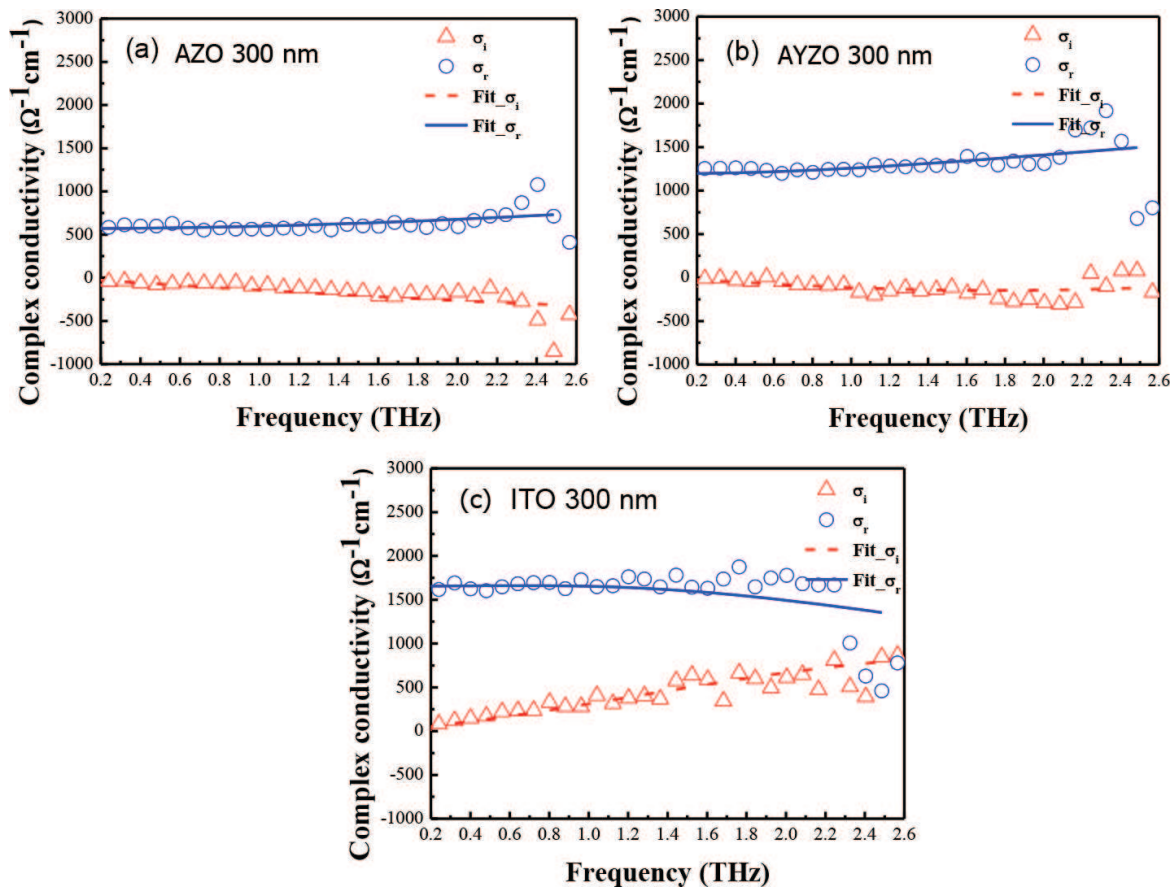
Figure 8. Real (blue circles) and imaginary (red triangles) parts of conductivity of (a) AZO, (b) AYZO, and (c) ITO thin films with thickness of 300 nm. Solid and dashed line corresponds to the fitting results based on the Drude-Smith model. Adapted from Ref. [29]**.**
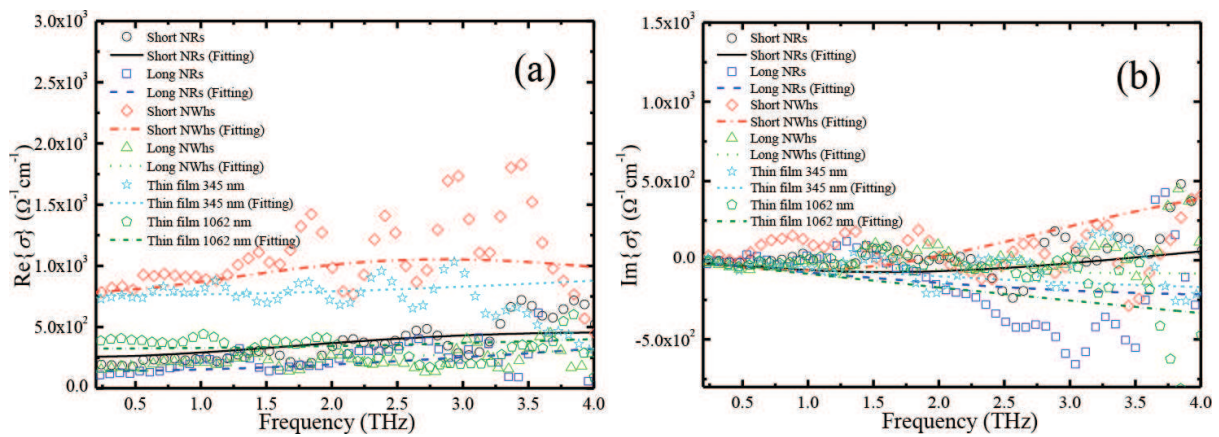
Figure 9. (a) Real and (b) imaginary conductivities of ITO nanomaterials (nanorods or NRs and nanowhiskers or NWhs) and thin films are plotted as a function of frequency (adapted from [13]). The symbols correspond to conductivities of samples extracted from THz-TDS measurements. The solid, dashed, dotted, and broken lines are fitting curves.

In **Figure 9**, we present complex conductivities of ITO nanomaterials and films studied by our group, reproduced from Ref. 13 by permission. The values of Re{σ} of both nanomaterials show a decreasing trend with frequencies in the THz band we studied. Regions of negative

values of Im{σ} are also observed. These are typical features associated with the materials that exhibit characteristics of carrier localization [2]. That is, the Drude-Smith model would likely be the model of choice. Indeed, Re{σ} and Im{σ} of ITO nanomaterials can be fitted well by this model (see **Figure 9**). From the fit, we determine that, for NRs with heights of 621.1 and 991.6 nm, the carrier scattering times are 31.7 and 13.5 fs; the plasma frequencies are 561 and 1006 rad THz; while the parameters γ are −0.71 and −0.88, respectively. Similarly, for the NWhs with heights of 802.6 and 1169.5 nm, we find that the carrier scattering times are 39.6 and 13.2 fs; the plasma frequencies are 751 and 853 rad THz; the parameters γ are −0.60 versus −0.74, respectively. All γ values of nanostructured ITO studied by our group are nearly −1.00. Such values of γ indicate that carrier localization effects in ITO NRs and NWhs are very important [13].

5. Liquid crystal terahertz phase shifters with functional ITO Nanomaterials

5.1. Introduction

By now, the potential of THz science and technology to a host of applications ranging from fundamental sciences to national security is well known [30]. Consequently, key components, such as phase shifters, modulators, filters, and polarizers, need to be developed. Liquid crystals (LCs) can be used to add functionalities to various THz optical and optoelectronic components [31–33]. We have previously shown that phase shifts exceeding 2π at 1 THz can be achieved by using electrically controlled birefringence in a homeotropically aligned LC (E7, Merck) cell, 1.83 mm in thickness and biased at 100 V_{rms} [33]. As ITO films are opaque in the THz frequency range [2, 13], we employed two copper pieces separated by ~11 mm at two sides of LCs' cell as electrodes for biasing and spacers [33].

As we illustrated in previous sections, the ITO NWhs can be used as transparent electrodes for THz applications [2, 13]. Indeed, we demonstrated THz phase shifters with a phase shift of around $\pi/2$ at 1.0 THz with ITO NWhs used as transparent electrodes [34, 35]. Significantly, ITO NWhs can also be used to align the liquid crystal molecules. Therefore, traditional alignment layers and procedures are not required.

In this section of the chapter, we present several designs of THz phase shifters with maximum phase shifts exceeding 2π or 360°. This is significant for applications such as phased array radar in the submillimeter band. ITO nanomaterials described in this work were employed as transparent electrodes. These devices can be operated at relatively low voltage and exhibit outstanding transmittance in the THz frequency region.

5.2. Construction of the THz phase shifters

Three possible designs are presented in **Figure 10**. In all, the LC (MDA-00-3461 by Merck) layers were sandwiched between fused silica substrates that have the inner surface (facing the LC layer) either deposited with or without ITO NWhs. Polyimides were deposited and rubbed for LC alignment. Before turning on the voltage biasing the ITO NWhs, the LC molecules are aligned parallel to the substrates. As the bias is increased beyond the threshold field due to the Fréedericksz transition, LC molecules will be reoriented toward the direction
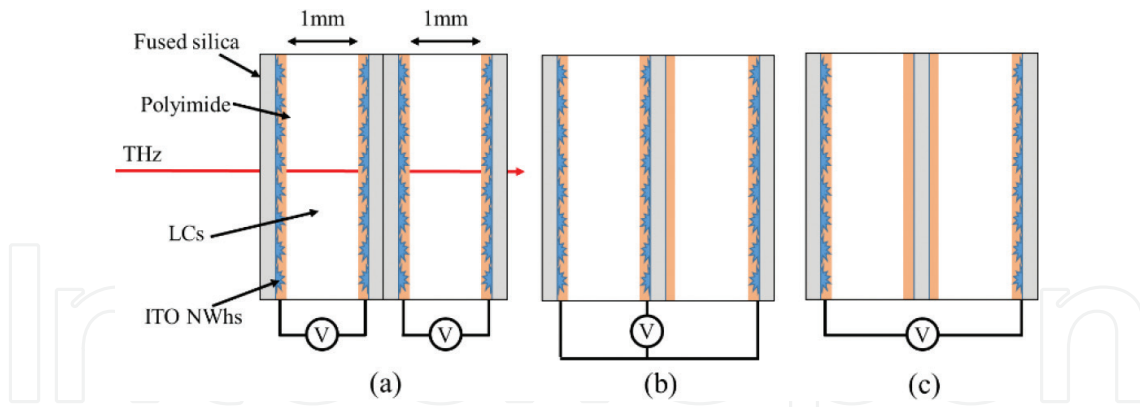
Figure 10. Schematic diagram of ITO NWhs 2π THz phase shifters in the (a) four-layer, (b) three-layer, and (c) two-layer design.

of the applied electric field. The threshold field is given by $E_{th} = \pi(k_1/(\varepsilon_0\Delta\varepsilon))^{1/2}/d$, where the free-space permittivity $\varepsilon_0 = 8.854 \times 10^{-12}$ F m^{-1} and d is thickness of a single cell or the distance between two electrodes as shown in **Figure 10**. The threshold field also depends on the splay elastic constant $k_1 = 12.6 \times 10^{-12}$ N and dielectric anisotropy, $\Delta\varepsilon = \varepsilon_{//} - \varepsilon_{\perp} = 11.2$ for this LC. After numerically finding the maximum tilt angle existing at every layer due to the weak boundary of substrates for LCs molecules, due to the effective birefringence, the phase shift can be given by $\delta = 2\pi f d\Delta n_{eff.Max}/c$, where f and c are the THz frequency and the speed of light in vacuum, respectively.

5.3. Results and discussions

All the three designs are found to be successful as THz phase shifters. In **Figure 11(a)**, we showed measured phase shifts of the devices as a function of the driving voltage. Phase shift exceeding 2π was demonstrated for all devices at 1.05 THz. The driving voltage needed is as low as 5 V$_{rms}$. Recalling performance of our previous work [33], the required voltage is lower by 20 times. Examining **Figure 1**, one immediately see that the threshold voltage is also quite low, less than 2 V$_{rms}$. Transmittance of all three phase shifters in the range of 0.2–1.2 THz is
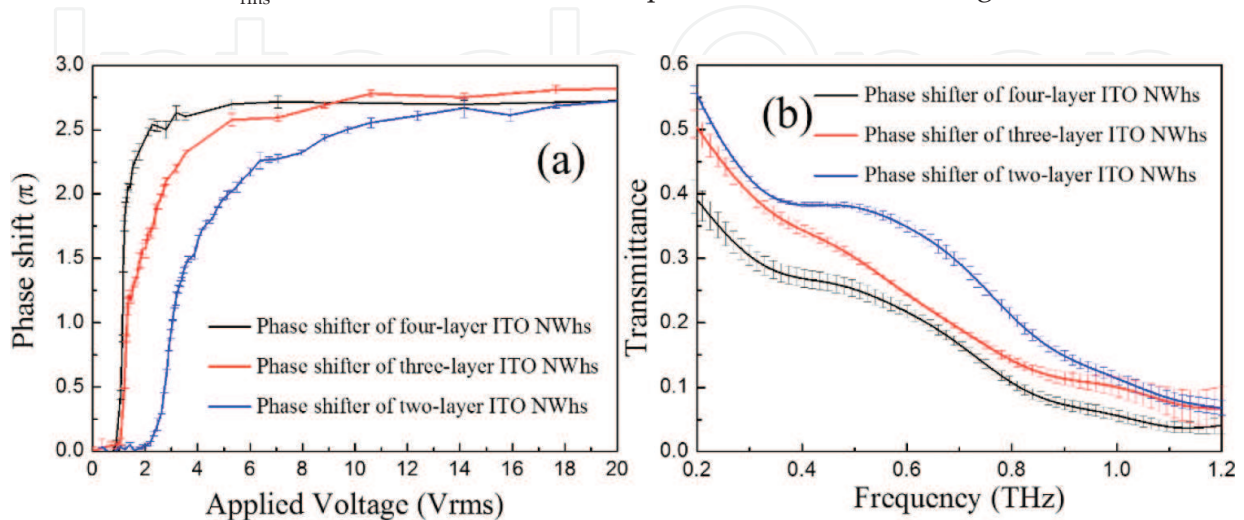
Figure 11. (a) Voltage-controlled phase shifts at 1 THz and (b) transmittance for three different 2π THz phase shifters based on multilayer ITO NWhs.

presented in **Figure 11(b)**. Note that the design with four layers of ITO NWhs exhibits the lowest threshold voltage and the lowest driving voltage needed to achieve 360° of phase shift. In contrast, the THz transmittance of the phase shifter with just two layers of ITO NWhs is significantly higher than others two. Although the loss of ITO NWhs is not so high in the THz frequency band, the accumulated loss of the device with the employment of more layers of electrodes is significant.

6. Summary

We have studied the frequency-dependent complex conductivities of several TCOs which have the potential in the THz applications. These include ITO nanomaterials, ITO sputtering films, AZO, and AYZO thin films. Methods for fabrication and characterization of these technologically important materials are described in detail. It is shown that ITO nanomaterials exhibit non-Drude-like electrical characteristics. Among the bulk films, AYZO has acceptable THz transmittance and good electrical properties such that it may be the better choice than the ITO and AZO thin films for optoelectronic applications in the THz band. Correlating with X-ray diffraction studies, we understood that the characteristics mentioned above can be explained by the extent of carrier localization in these materials. In comparison with the bulk films, ITO nanowhiskers are shown to be the material of choice as transparent electrodes in the THz band. To demonstrate, we show that the phase shifter using ITO NWhs exhibits transmittance as high as ~78% in the millimeter and submillimeter band. Several designs of the phase shifter using liquid crystal for tuning were demonstrated. Over 2π of phase shifts were realized at driving voltages that are over twenty times lower than previous designs.

Acknowledgements

Author details

Ci-Ling Pan[1]*, Chan-Shan Yang[1], Ru-Pin Pan[2], Peichen Yu[3] and Gong-Ru Lin[4]

*Address all correspondence to: clpan@phys.nthu.edu.tw

1 Department of Physics, National Tsing Hua University, Hsinchu, Taiwan

2 Department of Electrophysics, National Chiao Tung University, Hsinchu, Taiwan

3 Department of Photonics, National Chiao Tung University, Hsinchu, Taiwan

4 Graduate Institute of Photonics and Optoelectronics, National Taiwan University, Taipei, Taiwan

References

[1] G. Xu, Z. Liu, J. Ma, B. Liu, S.-T. Ho, L. Wang, P. Zhu, T. J. Marks, J. Luo, and Alex K. Y. Jen, "Organic electro-optics modulator using transparent conducting oxides as electrodes," Opt. Express 13, 7380–7385 (2005).

[2] C.-S. Yang, M.-H. Lin, C.-H. Chang, P. Yu, J.-M. Shieh, C.-H. Shen, O. Wada, and C.-L. Pan, "Non-Drude behavior in indium-tin-oxide nanowhiskers and thin films by transmission and reflection THz time-domain spectroscopy," IEEE J. Quantum Electron. 49(8), 677–690 (2013).

[3] P. Yu, C.-H. Chang, M.-S. Su, M.-H. Hsu, and K.-H. Wei, "Embedded indium-tin-oxide nanoelectrodes for efficiency and lifetime enhancement of polymer-based solar cells," Appl. Phys. Lett. 96, 153307 (2010).

[4] H. Yumoto, T. Sako, Y. Gotoh, K. Nishiyama, and T. Kaneko, "Growth mechanism of vapor–liquid-solid (VLS) grown indium tin oxide (ITO) whiskers along the substrate," Journal of Crystal Growth 203, 136–140 (1999).

[5] C.-W. Chen, Y.-C. Lin, C. H. Chang, P. Yu, J.-M. Shieh, and C.-L. Pan, "Frequency-dependent complex conductivities and dielectric responses of indium tin oxide thin films from the visible to the far-infrared," IEEE J. Quantum Electron. 46(12), 1746–1754 (2010).

[6] E. C. Garnett and P. Yang, "Silicon nanowire radial p-n junction solar cells," J. Am. Chem. Soc. 130, 9224–9225 (2008).

[7] M. D. Kelzenberg, S. W. Boettcher, J. A. Petykiewicz, D. B. Turner-Evans, M. C. Putnam, E. L. Warren, J. M. Spurgeon, R. M. Briggs, N. S. Lewis, and H. A. Atwater, "Enhanced absorption and carrier collection in Si wire arrays for photovoltaic applications," Nature Materials 9, 239–244 (2010).

[8] R. F. Bunshah and R. S. Juntz, "Influence of condensation temperature on microstructure and tensile properties of titanium sheet produced by high-rate physical vapor deposition process," Metallurgical Transactions 4, 21 (1973).

[9] H. Yumoto, J. Hatano, T. Watanabe, K. Fujikawa, and H. Sato, "Properties and surface morphology of indium tin oxide films prepared by electron shower method," Jpn. J. Appl. Phys. 32(part 1) 1204–1209 (1993).

[10] N. Laman and D. Grischkowsky, "Terahertz conductivity of thin metal films," Appl. Phys. Lett. 93, 051105 (2008).

[11] J. B. Baxter and C. A. Schmuttenmaer, "Conductivity of ZnO nanowires, nanoparticles, and thin films using time-resolved terahertz spectroscopy," J. Phys. Chem. B 110, 25229–25239 (2006).

[12] C. A. Schmuttenmaer, "Using terahertz spectroscopy to study nanomaterials," Terahertz Science and Technology 1, No. 1–8 (2008).

[13] C.-S. Yang, C.-M. Chang, P.-H. Chen, P. Yu, and C.-L. Pan, "Broadband terahertz conductivity and optical transmission of indium-tin-oxide (ITO) nanomaterials," Opt. Express 21(14), 16670–16682 (2013).

[14] C.-S. Yang, C.-H. Chang, M.-H. Lin, P. Yu, O. Wada, and C.-L. Pan, "THz conductivities of indium-tin-oxide nanowhiskers as graded-refractive-index structure," Opt. Express 20(S4), A441-A451 (2012).

[15] C.-S. Yang, C.-J. Lin, R.-P. Pan, C. T. Que, K. Yamamoto, M. Tani, and C.-L. Pan, "The complex refractive indices of the liquid crystal mixture E7 in the terahertz frequency range," J. Opt. Soc. Am. B 27(9), 1866–1873 (2010).

[16] J. Han, Z. Zhu, S. Ray, A. K. Azad, W. Zhang, M. He, S. Li, and Y. Zhao, "Optical and dielectric properties of ZnO tetrapod structures at terahertz frequencies," Appl. Phys. Lett., 89, 031107 (2006).

[17] J. Han, W. Zhang, W. Chen, S. Ray, J. Zhang, M. He, A. K. Azad, and Z. Zhu, "Terahertz dielectric properties and low-frequency phonon resonances of ZnO nanostructures," J. Phys. Chem. C, 111(35), 13000–13006 (2007).

[18] X. Zou, J. Luo, D. Lee, C. Cheng, D. Springer, S. K. Nair, S. A. Cheong, H. J. Fan, and E. E. M. Chia, "Temperature-dependent terahertz conductivity of tin oxide nanowire films," J. Phys. D: Appl. Phys., 45, 465101 (2012).

[19] G. J. Exarhos and X.-D. Zhou, "Discovery-based design of transparent conducting oxide films," Thin Solid Films, 515, 7025–7052 (2007).

[20] N. V. Smith, "Classical generalization of the Drude formula for the optical conductivity," Phys. Rev. B, 64, 155106 (2001).

[21] D. G. Cooke, A. N. MacDonald, A. Hryciw, J. Wang, Q. Li, A. Meldrum, and F. A. Hegmann, "Transient terahertz conductivity in photoexcited silicon nanocrystal films," Phys. Rev. B, 73, 193311 (2006).

[22] T. L. Cocker, L. V. Titova, S. Fourmaux, H.-C. Bandulet, D. Brassard, J.-C. Kieffer, M. A. El Khakani, and F. A. Hegmann, "Terahertz conductivity of the metal-insulator transition in a nanogranular VO$_2$ film," Appl. Phys. Lett., 97, 221905 (2010).

[23] H. Němec, P. Kužel, and V. Sundström, "Far-infrared response of free charge carriers localized in semiconductor nanoparticles," Phys. Rev. B, 79, 115309 (2009).

[24] H. Němec, P. Kužel, and V. Sundström, "Charge transport in nanostructured materials for solar energy conversion studied by time-resolved terahertz spectroscopy," J. Photoch. Photobio. A, 215, 123–139 (2010).

[25] L. V. Titova, T. L. Cocker, D. G. Cooke, X. Wang, A. Meldrum, and F. A. Hegmann, "Ultrafast percolative transport dynamics in silicon nanocrystal films," Phys. Rev. B, 83, 085403 (2011).

[26] E. Conwell and V. F. Weisskopf, "Theory of impurity scattering in semiconductor," Phys. Rev., 77(3), 388–390 (1950).

[27] J. Ederth, "Electrical transport in nanoparticle thin films of gold and indium tin oxide," Ph.D. dissertation, Dept. Mat. Science, Uppsala University, Uppsala, Sweden, 2003.

[28] J. Gao, R. Chen, D. H. Lin, L. Jiang, J. C. Ye, X. C. Ma, X. D. Chen, Q. H. Xiong, H. D. Sun, and T. Wu, "UV light emitting transparent conducting tin-doped indium oxide (ITO) nanowires," Nanotechnology, 22, 195706 (2011).

[29] C.-L. Pan and C.-S. Yang, "Transparent Conducting Oxides for THz Applications," The 8th International Photonics and OptoElectronics Meetings (POEM 2015), OSA Topical Meeting on Optoelectronic Devices and Integration (ODEI), June 16-19. Wuhan, China, paper OTB.1.

[30] X.-C. Zhang and J. Xu, Introduction to THz Wave Photonics, Springer, New York, US, 2010.

[31] C.-Y. Chen, C.-F. Hsieh, Y.-F. Lin, R.-P. Pan, and C.-L. Pan, "Magnetically tunable room-temperature 2π liquid crystal terahertz phase shifter," Opt. Express 12, 2630–2635 (2004).

[32] C.-F. Hsieh, R.-P. Pan, T.-T. Tang, H.-L. Chen, and C.-L. Pan, "Voltage-controlled liquid-crystal terahertz phase shifter and quarter-wave plate," Opt. Lett. 31, 1112–1114 (2006).

[33] H.-Y. Wu, C.-F. Hsieh, T.-T. Tang, R.-P. Pan, and C.-L. Pan, "Electrically tunable room-temperature 2π liquid crystal terahertz phase shifter," IEEE Photonic Technol. Lett. 18, 1488–1490 (2006).

[34] C.-S. Yang, T.-T. Tang, P.-H. Chen, R.-P. Pan, P. Yu, and C.-L. Pan, "Voltage-controlled liquid-crystal terahertz phase shifter with indium-tin-oxide nanowhiskers as transparent electrodes," Opt. Lett. 39(8), 2511–2513 (2014).

[35] C.-S. Yang, T.-T. Tang, R.-P. Pan, P. Yu, and C.-L. Pan, "Liquid crystal terahertz phase shifters with functional indium-tin-oxide nanostructures for biasing and alignment," Appl. Phys. Lett. 104, 141106 (2014).